# Measuring Velocity and Turbulent Diffusivity in Wall-Flow Filters using Compressed Sensing Magnetic Resonance

J.D. Cooper[a], A.P.E. York[b], A.J. Sederman[a], L.F. Gladden[a]*

[a] Department of Chemical Engineering and Biotechnology, University of Cambridge, West Cambridge Site, Philippa Fawcett Drive, Cambridge CB3 0AS, UK

[b] Johnson Matthey Technology Centre, Blounts Court, Sonning Common, Reading RG4 9NH, UK

* corresponding author (lfg1@cam.ac.uk)

Submitted: 11 June 2018

Revised: 7 August 2018

**Abstract**

Gas-phase compressed sensing magnetic resonance methods have been used to image gas flow velocity and turbulent diffusivity in wall-flow particulate filters. Two-dimensional magnetic resonance velocity imaging was used to observe the local distribution of gas velocity in the direction of superficial flow ($z$) in the entrance and exit regions of the filter at an in-plane spatial resolution of 140 µm ($x$) × 140 µm ($y$) and 140 µm ($x$) × 390 µm ($z$) perpendicular to and parallel with the direction of superficial flow, respectively. Images were acquired in 14 min. Three-dimensional images of the turbulent diffusivity were acquired at a spatial resolution of 286 µm ($x$) × 286 µm ($y$) × 1300 µm ($z$) for channel Reynolds numbers, $Re_c$ , of 210, 360, 720 and 1140. These data provide evidence of regions of turbulence inside the filter that has not been predicted by earlier numerical simulations. For $Re_c$ = 1140, a three-dimensional velocity image was also obtained at the same spatial resolution as the image of turbulent diffusivity; the data acquisition time was 2 h. Co-registration of these two images enables visualisation of the spatial extent and magnitude of these two characteristics of the flow field.

**Keywords**

particulate filter; turbulence; flow; turbulent diffusivity; magnetic resonance imaging

## 1. Introduction

### 1.1. Wall-flow particulate filters

Internal combustion engines produce many undesirable substances during operation that pose environmental and public health risks, including oxides of nitrogen (NOx), unburnt hydrocarbons and carbon monoxide, and particulate matter (PM). Of these, PM poses a unique set of problems since it typically comprises small carbonaceous particles with sizes ranging from the nanometre to micrometre scale, formed by incomplete combustion of fuel following imperfect mixing of atomised fuel and oxygen in the engine cylinders. Optimisation of engine designs has reduced the number of particulate emissions in both diesel and gasoline engines, but recent legislation such as the Euro 6 directive [1] has meant that on-board emission control systems are needed to comply with stricter limits. Diesel engines have traditionally produced more PM than gasoline engines, hence the diesel particulate filter (DPF) is the most commonly used technology to reduce PM emissions. However, more recently there has been a significant interest in the development of gasoline particulate filters (GPFs).

Both DPFs and GPFs can take different forms, though the most usual setup is a wall-flow filter formed from a porous ceramic monolith, made of cordierite, silicon carbide or aluminium titanate due to their favourable thermal and mechanical properties. Figure 1 shows a schematic of a wall-flow particulate filter. The monolith comprises several parallel channels, with alternating channels plugged at opposite ends to create a ‘checkerboard’ pattern. This structure forces the exhaust gas to pass through the permeable monolith walls, depositing the PM in the pores and allowing the gaseous components to pass through. As the filter operates, the walls become loaded with soot which, while increasing the efficiency of

filtration also increases the backpressures in the engine and reduces fuel efficiency. Regeneration of these filters requires oxidation of the trapped PM. This is achieved by either heating the exhaust gases to facilitate combustion with oxygen, or by exploiting the $NO_2$ present to oxidise the PM at a lower temperature. The optimal conditions for filter operation are often considered as a balance between maximising efficiency of filtration and minimising backpressure. Filters containing catalysts also require consideration of the conversion of gaseous pollutants.

In order to optimise the design of both wall-flow filters and the models used to predict their behaviour, an understanding of the flow phenomena at the entrance to and exit from the filters is essential. Measuring the local flow behaviours inside filter monoliths is a challenging problem and most work over the past 30 years has focused on numerical modelling of the flow. The initial work of Bissett [2] reported a 1D model of transport inside a DPF, and most subsequent models have been based at least partially on this work [3]. Simulations have since grown in complexity [4-8] and are the primary method for optimising the structure and operation of vehicle-mounted wall-flow filters. Validation of these models is typically via comparison of model predictions with macroscopic measurements, such as pressure drop [4,5], inlet and outlet gas temperatures [6], and outlet NOx concentrations [7]. Despite good agreement, this approach treats the filter as a black-box and offers little insight into the local flow behaviour.

The pressure drop across a filter is influenced by the hydrodynamics of the gas flow in the system. Masoudi [8] decomposed the pressure drop into 4 main contributions: Darcy flow through the walls and soot, axial flow along the channels, contraction effects at the entrance and expansion effects at the exit. The entrance and exit effects were reported to be

significant; their contribution to the pressure drop being up to 10% for moderately soot-loaded filters and between 25 – 50% for clean or lightly loaded filters. However, Watling et al. [9] reported no agreement between literature models regarding the relative contribution of the entrance and exit effects to the overall pressure drop. These effects are typically modelled using empirical correlations based on flow through abrupt cross-sectional area changes [10,11] and perforated plates [12,13], but such models do not capture the complex geometry and multi-channel nature of filters. Further, most models do not consider the flow profiles inside channels and the effects of flow maldistributions in such channels on heat and mass transfer [14,15]. A small number of three-dimensional simulations have been performed to study the contraction and expansion of gas at the ends of filters, notably by Konstandopoulos et al. [16] and Liu and Miller [17]. Both studies report broadly similar flow features as shown schematically in Fig. 1. These effects were predicted to influence the flow fields inside the channels, with potential reductions to filtration efficiency. To date there has been no experimental validation of these predictions beyond comparisons with pressure drop measurements. Hence, an understanding of the flow phenomena in these areas is needed for accurate modelling and prediction of filter behaviour.

The structure and composition of wall-flow filters make most conventional velocity measurement methods challenging. Optical methods, such as laser Doppler anemometry (LDA) and particle image velocimetry (PIV) are unsuitable due to the opaqueness and geometry of the filter, while hot wire anemometry (HWA) is highly invasive. This study uses magnetic resonance (MR) techniques to study the gas flow directly. MR is a non-invasive imaging modality which provides sub-channel spatial resolution and motion encoding, and can be used to study optically opaque samples.

The motivation for the present work is to develop and demonstrate the ability of magnetic resonance methods to measure the flow velocities and turbulent diffusivity at the entrance to, and exit from, the monolith and to characterise hydrodynamics along the length of the channels. In ongoing work, such data are being used to aid the development of computational codes which predict the flow behaviour and pressure drop characteristics of the filters. Improvement in the accuracy of these predictions will, in turn, aid the ability to predict and design the filtration, regeneration and catalytic performance of wall-flow filters.

### 1.2. Magnetic resonance measurements of fluid motion

In this section, a brief description of MR is given in relation to the measurement of motion. A more thorough treatment of MR measurements of fluid transport is given by Callaghan [18].

Magnetic resonance probes the nuclei of atoms with non-zero nuclear spin, such as $^{1}$H or $^{19}$F, by measuring the precession of such spins in a strong magnetic field; the frequency of precession, $\omega$, is directly proportional to the magnetic field strength, $B_0$:

$$\omega = \gamma B_0, \#(1)$$

where $\gamma$ is the gyromagnetic ratio of the nucleus. The complex MR signal is acquired as an ensemble sum of individual spins, permitting the phase and magnitude of the bulk signal to be recovered. The frequency of the precession is made spatially-dependent by applying a magnetic field gradient $\mathbf{G}$ across the sample, such that a spin at position $\mathbf{r}$ experiences an additional field $\mathbf{r} \cdot \mathbf{G}$ and precesses at a frequency offset, $\Delta\omega$:

$$\Delta\omega(\mathbf{r}) = \gamma \mathbf{r} \cdot \mathbf{G} \,. \#(2)$$

The phase is the integral of the frequency over time, and can be written in terms of the applied gradient $\mathbf{G}(t)$ and the Taylor expansion of spin position $\mathbf{r}(t)$:

$$\phi = \gamma \int \mathbf{r}(t) \cdot \mathbf{G}(t)\, \mathrm{d}t = \gamma \left[ \mathbf{r} \cdot \underbrace{\int \mathbf{G}(t)\, \mathrm{d}t}_{M_0} + \frac{\mathrm{d}\mathbf{r}}{\mathrm{d}t} \cdot \underbrace{\int \mathbf{G}(t)\, t\, \mathrm{d}t}_{M_1} + \cdots \right], \#(3)$$

where $M_0$ and $M_1$ are the zeroth and first gradient moments; higher order moments are typically negligible and can be ignored. Application of magnetic field gradient pulses leads to non-zero gradient moments and hence a dependence of the phase on initial position, $\boldsymbol{r}$, and velocity, $\frac{\mathrm{d}\boldsymbol{r}}{\mathrm{d}t}$. Conventional MR imaging (MRI) experiments use a sequence of gradients to modulate the zeroth moment in order to encode spatial position in the phase. By designing a sequence of gradient pulses such that the zeroth moment is nulled and the first moment is non-zero, the signal phase can be made directly proportional to the velocity and independent of the position. This sensitivity to position and velocity can be combined, permitting the acquisition of spatially-resolved velocity maps.

The velocity of a fluid can be decomposed into two components, $v(t) = \bar{v} + v'(t)$, where $\bar{v}$ is the time-independent mean velocity and $v'(t)$ describes the time-dependent velocity fluctuations associated with turbulence. In the context of the current work, it is of interest to measure both velocity terms. The velocity fluctuations result in a distribution of spin phases, with a dispersion related to that of the velocity. The size of the velocity fluctuations, referred to as the velocity dispersion, is expected to increase with increasing turbulence. The principles of the MR measurement are now summarised. For two gradient pulses of length $\delta$,

the first of strength $+g$ and the second $-g$, and time separation Δ (commonly referred to as the observation time), the phase of this bulk signal, Φ, is proportional to the mean velocity, $\bar{v}$:

$$\Phi = \gamma g \delta \Delta \bar{v}. \#(4)$$

Hence, quantitative velocity maps can be calculated from the signal phase. The dispersion of the phase distribution causes an attenuation of the bulk signal magnitude, $S$, with the mean square phase, $\langle \phi^2 \rangle$:

$$S = S_0 \exp\left[-\frac{\langle \phi^2 \rangle}{2}\right], \# (5)$$

where $S_0$ is the signal expected in the absence of phase dispersion.

Several models have been developed that relate the mean square phase of the signal to the fluid behaviour [19–23]. In particular, Kuethe and Gao [23] have shown that when the timescale of the velocity fluctuations is short compared to Δ, the effect of turbulence on the MR signal resembles Brownian diffusion and can be characterised using the 'eddy diffusivity' or 'turbulent diffusivity,' $D_{turb}$:

$$\langle \phi^2 \rangle = 2\gamma^2 g^2 \delta^2 \left(\Delta - \frac{\delta}{3}\right) D_{turb}. \#(6)$$

In the opposite limit, where the timescale of the velocity fluctuations is large compared to Δ, the mean square phase scales as $\Delta^2$ [19]. It follows that, if the logarithm of the signal decays linearly with Δ, then the velocity fluctuations are uncorrelated over the timescale Δ and Eq. (6) is valid. By substituting Eq. (6) into Eq. (5), the Stejskal-Tanner equation, commonly used in the measurement of self-diffusion coefficients, is obtained [24]. The turbulent diffusivity is calculated by considering the log difference between two datasets measured with static and flowing fluids respectively:

$$D_{turb} = \frac{\log[S_0] - \log[S]}{\gamma^2 g^2 \delta^2 \left(\Delta - \frac{\delta}{3}\right)}, \#(7)$$

and is related to the mean square velocity fluctuation, or the turbulent kinetic energy, $\langle v'^2 \rangle$, by the Lagrangian correlation time $\tau_c$ [25]:

$$D_{turb} = \tau_c \langle v'^2 \rangle. \#(8)$$

MRI and MR velocity imaging has been used to study a range of flowing systems and interested readers are directed to reviews by Newling [26] and Gladden and Sederman [27,28]. The majority of work in this field has addressed the imaging of liquid flow fields, while the study of gases and their flows are less common. The main reasons for this are twofold; gases have a much lower molecular density than liquids, leading to a low signal-to-noise ratio (SNR), and a much larger self-diffusion coefficient, leading to a reduced signal lifetime, image blurring and decreased velocity resolution. However, there is increasing interest in the development and implementation of gas-phase MRI and velocity mapping in engineering systems [26,28].

With respect to the imaging of fluid flows in monoliths, gas flow has been indirectly measured in ceramic monoliths [29–31] through imaging the liquid content of two phase flows. Koptyug and co-workers demonstrated both the feasibility of using thermally polarised hydrocarbon gases to directly follow gas phase flows and their application to a flow-through monolith [32]. More recently, Ramskill and colleagues demonstrated the measurement of liquid flow [33] and gas flow [34] in DPFs. In the latter study, $SF_6$ was chosen for its favourable MR relaxation times, low self-diffusion coefficient and high sensitivity.

The study of turbulent flows using MR techniques has largely followed two routes: ‘snap-shot’ imaging at a timescale well below the correlation time of the fluid, showing an almost-instantaneous picture of the eddies and vortices with either phase or signal attenuation contrast [35,36], and time-averaged studies, looking at the system over an extended period of time to identify regions with higher and lower turbulence. Snap-shot methods provide great insight but are difficult to implement, requiring high sensitivity, optimal relaxation times and excellent magnetic field homogeneity. Time-averaged studies of turbulence offer a more applicable method and allow more systems to be studied, examples include a jet of water exiting a nozzle [25], water flowing through a stenosis [37], and $SF_6$ gas flow over a bluff obstruction and a wing section [38].

Validation of time-averaged MR studies of turbulence has been addressed by comparison of MR data with other anemometry techniques. In particular, Elkins et al. [39] found good agreement between MR and PIV measurements of velocity in turbulent flows, while O'Brien et al. [40] reported that short echo times in the MR acquisition minimise flow artefacts and increase agreement with LDA methods. The effects of intra-voxel velocity and noise on MRI turbulence measurements were studied by Dyverfeldt et al. [41], showing that while the former has no significant impact, the strength of the motion encoding gradients needs to be optimised relative to the noise level in the image to minimise uncertainty and undermeasurement.

The present work builds on the analysis and methods of Kuethe [25] and Newling et al. [38] and applies them to study turbulent flows in a wall-flow filter system. Phase-encoded MR methods are used to minimise artefacts from flow and magnetic field inhomogeneities, as well as maximising the potential for employing compressed sensing (CS) methods.

Developed by Lustig et al. [42], CS has become established as a robust method for reducing MR acquisition times through sampling fewer data without reducing image fidelity or quantification [43,44]. Two-dimensional (2D) and three-dimensional (3D) MR imaging methods were employed to measure the gas velocity and turbulent diffusivity. Gas flow rates characterised by channel Reynolds numbers, $Re_c$, in the range 210-1140 were considered which include those experienced in fitted filters for a range of driving styles ($Re_c$ = 100 – 1000).

## 2. Experimental

### 2.1. Materials and equipment

In this study, a cylindrical sample of an aluminium titanate DPF was used; the details of which are given in Table 1. In all experiments, only the channels with 8 neighbouring channels are used for analysis in order that all channels are subject to the same boundary conditions (i.e., wall-effects are minimised). The sample was held in a cylindrical polyetheretherketone (PEEK) cell, of internal diameter 18 mm, that operates at pressures up to 10 bar(g) (Fig. 2). Gas was delivered to the PEEK cell through a ⅛″ diameter tube (Swagelok); expansion into the PEEK cell occurred 50 mm ahead of the entrance to the filter, resulting in an approximately uniform entrance condition to the filter. At the exit, gas leaves the filter and enters the PEEK cell; at 100 mm from the filter exit the exit geometry tapers down to a ⅛″ diameter tube (Swagelok) over a distance of 20 mm. The sides of the filter were wrapped in PTFE tape to avoid gas bypassing the filter by passing between the filter and the inner walls of the PEEK cell.

Sulfur hexafluoride ($SF_6$) was chosen as the MR-active gas for its favourable properties for MR velocity imaging, as described in Sankey et al. [45]. Use of $SF_6$ allows MR experiments

to be performed with thermally-polarised (i.e. as-received) gas, thereby avoiding the need for hyperpolarisation of gases such as $^{129}Xe$ and $^{3}He$ which is both technically demanding and results in MR data containing relaxation effects that are difficult to quantify. $SF_6$ was pressurised to 5.25±0.25 bar(g) in a closed recirculating rig, a schematic of which is shown in Fig. 3. The circuit consisted of a DILO Piccolo compressor (model B022R01), high and low pressure reservoirs, an upstream in-line pressure gauge, and a Bronkhurst mass flow controller (model F-113AC-M50-AAD-55-E). The mass flow rates used for the experiments were 25, 50, 100 and 150 g $min^{-1}$, corresponding to channel Reynolds numbers, $Re_c$, of 210, 360, 720 and 1140 respectively, where $Re_c$ is based on the average superficial velocity at the entrance of the inlet channels and the channel side-length. The experiments were performed at 21±1 °C.

### 2.2. Magnetic resonance

All magnetic resonance experiments were performed using a 9.4 T vertical bore superconducting magnetic controlled by a Bruker AV-400 spectrometer. The spectrometer was tuned to the $^{19}F$ resonance frequency, 376.6 MHz. A 25 mm birdcage coil was used for radiofrequency (r.f.) excitation and detection. Spatial resolution and motion encoding were achieved using three orthogonal microimaging gradients with a maximum strength of 146.1 G $cm^{-1}$ in each direction. A matrix rotation was applied to align the natural axes of the filter sample with those of the gradient coils. The short relaxation times of $SF_6$ ($T_2 \approx T_1 < 14$ ms at 6 bar(g)) allowed a recycle time of 32 ms to be used.

All experiments were based on a spin-echo single point imaging pulse sequence [34,46] shown in Fig. 4, with 128 complex points in the free induction decay acquired at a sweep width of 200 kHz and summed to increase the signal-to-noise ratio (SNR). Compressed

sensing methods were used for all acquisitions, allowing a decrease in sampling rates and hence acquisition times by a factor of 5 for the 2D images and a factor of 4 for the 3D images. Motion encoding was achieved using two gradient pulses either side of the 180° pulse (Fig. 4d).

2D velocity images of the velocity in the direction of superficial flow (z) were acquired on a 128 × 128 matrix with a field-of-view (FOV) of 18 mm × 18 mm for the *xy* images and 50 mm × 18 mm for the *xz* images, corresponding to an in-plane pixel resolution of 140 μm (*x*) × 140 μm (*y*) and 140 μm (*x*) × 390 μm (*z*) respectively. With reference to Fig. 4, spatial resolution was achieved using phase imaging gradients (Fig. 4c) in the two desired directions. Slice selection was obtained in the final direction using a 256 μs Gaussian-shaped soft 180° r.f. pulse and slice gradient (Figure 4a, b). The image slice thickness was 0.25 cm; in all figures, the spatial location of the image slice is identified as the position of the middle of the slice. The motion encoding gradient strength was ±1.46 G $cm^{-1}$, with duration 0.74 ms and an observation time 1.74 ms was used. The acquisition time of a 2D velocity image was 14 min.

3D turbulent diffusivity imaging was achieved through the addition of a third image phase gradient to the 2D imaging sequence. A 512 μs Hermite-shaped soft 180° r.f. pulse and slice gradient were used in the *z* direction to shorten the FOV and increase the axial resolution. Images were acquired on a 64 × 64 × 32 matrix with a FOV of 18 mm × 18 mm × 40 mm, yielding a voxel resolution of 286 μm (*x*) × 286 μm (*y*) × 1300 μm (*z*). Two images were acquired, one with and one without flow, with a motion encoding gradient strength and duration of 0.73 G $cm^{-1}$ and 0.74 ms, respectively, and an observation time 2 ms. The acquisition time for a single image was 1 h. For a $Re_c$ = 1140, a 3D velocity image was also acquired where 2 values of the velocity encoding gradient were used, with strengths ±0.73 G

$cm^{-1}$. The acquisition time for the complete 3D velocity image was 2 h. The spatial resolution and other experimental parameters are the same as those used for acquisition of the turbulent diffusivity images.

The MR signal is acquired as separate real and imaginary data, each with normally-distributed noise. This results in a Rician distribution of noise in the magnitude data and a complex, non-linear distribution in the phase data. It has been shown that for SNR > 3, both distributions are well approximated as normal distributions [47]. As the lowest SNR in this study was 6, this approximation is valid. The errors are quoted as the standard deviation of the uncertainty distribution of each measurement. The error in the 2D velocity measurements is calculated to be < 1.4 cm $s^{-1}$, while the error in the 3D velocity map is < 0.1 cm $s^{-1}$. The error in the measurement of $D_{turb}$ is < 0.03 $cm^2$ $s^{-1}$.

Prior to acquiring the velocity and turbulent diffusivity maps, it was confirmed that the turbulent motion of the spins is uncorrelated as required by the model of Kuethe [25], and hence Eq. (6) is used to determine $D_{turb}$. This was achieved by measuring the signal attenuation as a function of encoding time Δ with a constant gradient strength of 7.3 G $cm^{-1}$. The echo time, $T_E$, was kept constant to remove any outflow or relaxation weighting effects. The logarithm of the attenuation showed a linear dependence on evolution time, confirming the assumption of uncorrelated velocity fluctuations. This is consistent with the findings of Newling et al. [38].

### 2.3 Compressed Sensing Reconstruction

The undersampling method of Lustig et al. [42] was used to produce 2D and 3D undersampling patterns, generated with a polynomial probability density. The sampling

density is concentrated in the centre of *k*-space as this area contains the highest energy coefficients of the reconstructed image. The total variation ($TV(\boldsymbol{x}) = \|\nabla \boldsymbol{x}\|_2$) regulariser was chosen to reconstruct the undersampled 2D and 3D images as it offers good edge preservation [48]. The 2D reconstructions follow the methods reported in Ramskill et al. [34]. However, due to the lower resolution of the 3D images, a binary mask $\mathbf{M_b}$ was generated from fully-sampled images, acquired with 8 scans over 8 h, and used as an additional penalty term for the 3D images [44]. The overall reconstruction problem can be expressed as the minimisation:

$$\boldsymbol{x_\alpha} \in \text{argmin}_{\mathbf{x}} \left\{ \frac{1}{2} \|\boldsymbol{y} - S\boldsymbol{F}\boldsymbol{x}\|_2^2 + \alpha TV(\boldsymbol{x}) + \beta \|(1 - \mathbf{M_b}) \circ \boldsymbol{x}\|_2 \right\}, \#(9)$$

where $\boldsymbol{x}$ is the reconstructed image, $\boldsymbol{y}$ is the acquired undersampled data, $S$ is the undersampling pattern, $\circ$ is the element-wise Hagamard product, $\|\cdots\|_2$ is the Euclidean 2-norm and $\boldsymbol{F}$ is the discrete Fourier transform. The regularisation coefficients, $\alpha$ and $\beta$, were chosen heuristically. The reconstruction was performed using the in-house Object Orientated Mathematics for Inverse Problems (OOMFIP), implemented by Benning et al. [49].

### 2.4 Design of Experiments

Two sets of experiments were performed. First, 2D velocity-encoded images were acquired at $Re_c$ = 360 at the filter entrance and exit. Second, 3D turbulent diffusivity images were acquired at $Re_c$ = 210, 360, 720 and 1140. For $Re_c$ = 1140, a 3D velocity map was then recorded allowing co-registration of the 3D velocity and turbulent diffusivity images at this value of $Re_c$.

## 3. Results

The results are presented in two sections. First, Section 3.1 reports 2D velocity images of the *z*-component of velocity as gas enters and exits the wall-flow filter. Section 3.2 then reports

the 3D images of the turbulent diffusivity. The co-registered 3D images of velocity and turbulent diffusivity recorded for $Re_c$ = 1140 are also shown; this visualisation illustrates the power of the MR measurements to characterise the magnitude and extent of these flow characteristics and how they relate to each other.

### 3.1. Flow patterns at filter entrance and exit

2D velocity images were acquired to observe the local flow distributions of gas entering and exiting the filter for $Re_c$ = 360. For the *xy* images, the *z* distance indicates the position of the middle of the image slice.

Figures 5 and 6 show the images acquired of the z-component of the flow velocity, $v_z$, at entry to the filter. Figure 5 shows that the contraction of flow into the filter channels is smooth and well-behaved with no visible eddies present. Figures 5 b-d show the velocity profiles at 3 positions along the *z*-direction. The flow upstream of the filter is approximately uniform at ~6 cm $s^{-1}$ (Fig. 5b). At entry to the channels (Fig. 5c), the flow has a plug-flow profile which develops into a more laminar flow profile at 0.38 cm along the channel. The *xy* images shown in Fig. 6 also show clean contraction; the flow profile is largely uniform upstream of the filter (Fig. 6a) before contracting smoothly (Fig. 6b) and showing plug-flow behaviour inside the channels (Fig. 6c). The flow is seen to develop into a more parabolic profile further inside the filter (Fig. 6d), with the maximum velocities observed at the centre of the channels reaching ~19 cm $s^{-1}$.

Figure 7a shows an *xz* image of $v_z$ at the exit from the filter. The gas is seen to exit the channels as high-velocity jets, between which green and blue pixels are seen in the image identifying regions of slow, static and recirculating flow that extend about 0.4 cm downstream of the filter. Figures 7b-d show profiles of $v_z$ at the exit (Fig. 7b) and then at

positions 0.06 and 0.4 cm downstream of the exit, respectively. The jets are well-defined until about 0.35 cm downstream of the filter, where coalescence begins and continues to 1 cm downstream. The velocity images acquired in the *xy* plane (Fig. 8) allow assessment of the flow heterogeneity downstream of the filter. Figure 8a shows the laminar flow of gas in the channels. Variation in the flow velocity in individual channels is seen, consistent with the data shown in Fig. 7b. In contrast to the flow behaviour at the entrance, there is considerable heterogeneity in the flow at the exit from the filter. In Fig. 8b, taken at 0.25 cm downstream of the filter exit, whilst the jets are still clearly resolved there are also some regions of backflow between individual jets (again indicated by the blue/green shades). At 0.75 cm from the filter exit (Fig. 8c) significant jet coalescence has occurred, and coalescence increases up to the furthest distance studied at $z$ = 1.75 cm (Fig. 8e). However, even in this image evidence of a single jet remains. Also of note is a large region of negative velocity, indicating a recirculating flow, at the top-left of the images which spans several channels. Of course, large scale re-circulations will be influenced by the design of the monolith exit and downstream geometry, and this will be the subject of future work.

### 3.2. Magnetic resonance images of turbulent diffusivity

The images of turbulent diffusivity characterise the range of velocities existing within each voxel over the data acquisition time; laminar flow is expected to have a low range of velocities in a volume element and hence a small turbulent diffusivity, and vice versa for turbulent flow. Images of the turbulent diffusivity were acquired at the entrance and exit regions of the filter sample for each of $Re_c$ = 210, 360, 720 and 1140. Whilst the magnitude and spatial extent of the turbulent diffusivity increased with increase in $Re_c$, the general behaviour for all $Re_c$ was very similar. Figures 9 and 10 show 2D *xy* slices from the 3D dataset at the entrance and exit region respectively. Data are shown for $Re_c$ = 1140.

Figure 9a shows that turbulent diffusivity occurs ahead of the entry of the gas into the filter; these regions of turbulent flow occur ahead of the plugged regions between the inlet channels. In the image shown, 6 such regions are identified and are seen to be associated with $D_{turb}$ values of ~1.3-1.5 $cm^2 s^{-1}$. Further, there is evidence of turbulent diffusivity inside the channels (Fig. 9b, c), occurring adjacent to the channel walls. These regions of turbulent flow are not readily identified from the 2D flow velocity maps, such as that shown in Fig. 5a.

Figure 10 shows the maps of turbulent diffusivity at positions of 0.07, 0.20 and 0.33 cm from the filter exit. It is seen that immediately after the exit, significant turbulence is observed with the highest values occurring in the form of annuli where the high velocity gas leaving the filter interacts with the stagnant gas between the jets. These features in the flow exist to about 0.4 cm downstream from the filter exit, over a shorter range than the jets in the velocity field. Figure 11 shows co-registered images of the velocity and turbulent diffusivity. The jets shown in the velocity map again extend much further than the turbulent diffusivity. The 3D velocity dataset also revealed recirculating flows at the exit end of the inlet channels, as the flow meets the channel plugs.

The turbulent diffusivity distributions at both ends of the filter show some variation between individual channels, as is expected from the non-uniform gas flow shown in Fig. 5-8. In order to better understand the development of the turbulent diffusivity along the filter axis, the 3D datasets were projected onto the *z* axis through averaging along the *x* and *y* axes. The projections at the entrance and exit are shown in Fig. 12a and 12b, respectively, for $Re_c$ = 210, 360, 720 and 1140. At the entrance (Fig. 12a), two peaks (A and B) in the turbulent diffusivity are clearly seen at $Re_c$ = 720 and 1140. Some evidence of these two features is

also seen at $Re_c$ = 360. Peak A characterises the flow in the inlet channels over the length-scale of the plugs (in the adjacent outlet channels), consistent with the data shown in Fig. 9c. Peak B, however, exists beyond the limit of the plugged region; inspection of the 3D dataset allows us to assign this feature to flow in the inlet channels. Figure 12b shows the data obtained for the exit region. Again, 2 peaks in the turbulent diffusivity are observed. The larger peak (Peak C) exists in the outlet channels over the length-scale of the plugged region of the inlet channel. The smaller peak (Peak D) occurring at $z$ = 0.13 cm beyond the filter exit corresponds to the turbulent structure seen in Fig. 10a.

## 4. Discussion

CFD studies of entrance and exit effects in wall-flow filters are limited in number. Here, the MR results are compared with the predictions reported by Konstandopoulos et al. [16] for a square channel geometry ($Re_c$ = 530 - 2120) and Liu and Miller [17] for a triangular channel geometry ($Re_c$ = 186 - 1859); these simulations represent work in which the channel geometry and Re are closest to those studied in the present work. Both studies show broadly similar flow fields; the exit is composed of high velocity jets and recirculating regions behind the inlet channel plugs. However, there are some key differences between the two. At the entrance, Konstandopoulos et al. predicted completely smooth contraction of gas into the inlet channels, whereas Liu and Miller found recirculating flow developing in front of the plugs in the outlet channels. Similarly, at the exit Liu and Miller found that recirculations develop at the end of the inlet channels in front of the rear plugs. Konstandopoulos reported that the exit jets induced strong mixing and pressure fluctuations that continued for several plug lengths downstream of the filter. Both studies predicted the flow phenomena to be present at all flow rates considered in their simulations.

The MR data are in good agreement with the main predictions of these earlier workers. While the MR velocity maps (Fig. 5, 6) showed no recirculating flow at the entrance, the turbulent diffusivity maps (Fig. 9) do indicate turbulent flow occurring ahead of the inlet plugs as predicted by Liu and Miller [17]. Though not shown, negative axial velocities were observed at the end of the inlet channel, indicating recirculating flow, again confirming the predictions of Liu and Miller. Figure 6 shows the formation of jets at the exit as predicted in both studies. From Fig. 8, most exit jets coalesce within 1.5 cm of leaving the filter, but the flow field has not redeveloped fully by 2.5 cm and appears to be influenced by a larger recirculating feature. This may result in local pressure fluctuations for at least 5 plug lengths downstream, consistent with the observation of Konstandopoulos et al. Neither study predicted any unsteady flow that accounts for the additional turbulent diffusivity peaks (Peaks B and C) observed in Fig. 12 despite their significant contribution to the overall turbulent diffusivity. It is thought that these flow features may be caused by the high transverse velocity through the filter walls, which is greatest at the ends of the filters [34] and occurs suddenly due to the plugged structure of the filter.

Whilst generally good agreement is observed between the present MR data and the predictions of numerical simulations, the strict periodic boundary conditions used in CFD simulations enforces uniform flow in all channels which is not observed experimentally. Consideration of the distribution of flow from upstream of the filter helps explain the heterogeneities in flow seen in Fig. 5-8. Exhaust gas entering wall-flow filters is usually supplied from a much smaller exhaust tube that increases in diameter through a linear cone. CFD simulations of gas flow through the inlet cone [50–52] have predicted a large degree of inhomogeneity in the velocity distribution of gas as it enters the filter and large recirculating flow fields between the face of the filter and the cone, which has been observed using PIV by

Turner et al. [52]. Through simulations, Mu et al. [50] calculated 88% of the exhaust gas enters the central 53% of the filter, causing an inherent non-uniformity in the flow across the filter and impacting the filtration efficiency. This non-uniformity will also be present in the gas exiting the filter, as the velocity of gas in the filter is highly anisotropic [34], and will cause a non-uniform velocity distribution at the filter exit face. The MR methods presented here are well-positioned to explore such phenomena and hence aid the development of simulation codes in application to the design of wall-flow filters. Aspects of the inlet and outlet geometry to the filter are the subject of ongoing work.

## 5. Conclusions

In this study, compressed sensing spin-echo single point MR imaging of gas velocity and turbulent diffusivity have been demonstrated in application to the study of gas flow behaviour at the entrance and exit regions of a wall-flow filter. 2D velocity-encoded images of the flow velocity in the direction of the superficial flow were obtained in the *xz* and *xy* planes, at a nominal spatial resolution of 140 μm (*x*) × 390 μm (*y*) and 140 μm (*x*) × 140 μm (*z*) respectively, at both the filter entrance and exit. 2D velocity images were acquired in 14 min. Data are shown for $Re_c$ = 360. The evolution of flow velocity at the filter entrance is seen to be smooth, and the evolution of the flow in the inlet channels from plug to laminar flow is observed along the length of the channel. Some evidence of back flow at the end of the inlet channel in front of the plugged region was observed. At the filter exit, jets leaving the outlet channel are observed, as are regions of stagnant and recirculating gas at the face of the filter associated with the plugged inlet channels.

3D images of the local turbulent diffusivity distributions at the filter entrance and exit were acquired in under 1 h; with a spatial resolution of 280 μm (*x*) × 280 μm (*y*) × 1300 μm *(z*). At

the entrance, two distinct regions of turbulent diffusivity are identified. The first exists predominantly along the walls of the filter immediately after entry, whilst the second region is downstream of the plugged channels. Both regions of turbulence exist within the inlet channels. At the exit, significant turbulent diffusivity was observed before the filter exit (in the outlet channels) with a second region just beyond the filter exit where the high velocity exit jets interact with stagnant and recirculating flows present between the jets. The regions of turbulent diffusivity existing within the channels at both the filter entrance and exit have not been predicted by numerical simulations and are attributed to the flow through the walls of the filter. Co-registration of 3D images of gas velocity and turbulent diffusivity at the filter exit enables the spatial location and range of the flow velocity and turbulent diffusivity to be visualised at the filter exit.

MR images of velocity and turbulent diffusivity have provided experimental data which enable critical evaluation of the predictions of flow in a wall-flow filter. The MR data reveal not just the local, channel scale behaviour but also the macroscopic flow patterns beyond the limits of the filter. The MR data show the heterogeneous nature of the flow field and these methods can be used to explore the relationship between the geometry of the entrance and exit condition of the filter and how these interact with the design characteristics of the monolith itself.

**Acknowledgements**

JDC would like to thank Johnson Matthey and the EPSRC for a CASE award (award reference 1628588). The authors also wish to thank Dr Tim Watling (Johnson Matthey plc) for useful discussions on filter structure and operation.

**Nomenclature**

Abbreviations

| | |
|---|---|
| CS | compressed sensing |
| DPF | diesel particulate filter |
| FOV | field-of-view |
| GPF | gasoline particulate filter |
| HWA | hot wire anemometry |
| LDA | laser Doppler anemometry |
| MR | magnetic resonance |
| MRI | magnetic resonance imaging |
| NOx | nitrogen oxides |
| PEEK | polyetheretherketone |
| PIV | particle image velocimetry |
| PM | particulate matter |
| SNR | signal-to-noise ratio |

Latin Characters

| | |
|---|---|
| $B_0$ | magnetic field strength, T |
| $D_{turb}$ | turbulent diffusivity, $cm^2\ s^{-1}$ |
| $\boldsymbol{F}$ | discrete Fourier transform matrix |
| $g$ | magnetic field gradient strength, $G\ cm^{-1}$ |
| $\mathbf{G}$ | magnetic field gradient strength, $G\ cm^{-1}$ |
| $M_0$ | zeroth gradient moment, $G\ s\ cm^{-1}$ |
| $M_1$ | first gradient moment, $G\ s^2\ cm^{-1}$ |
| $\mathbf{M_b}$ | image binary mask |

| | |
|---|---|
| $\mathbf{r}$ | position, cm |
| $Re_c$ | channel Reynolds number |
| $S$ | MR signal |
| $S_0$ | MR signal in absence of flow |
| $S$ | undersampling pattern |
| $t$ | time, s |
| $T_1$ | longitudinal relaxation time, ms |
| $T_2$ | transverse relaxation time, ms |
| $T_E$ | echo time, ms |
| $TV$ | total variation regulariser |
| $v$ | velocity, cm $s^{-1}$ |
| $\bar{v}$ | mean velocity, cm $s^{-1}$ |
| $v'$ | velocity fluctuations, cm $s^{-1}$ |
| $\boldsymbol{x}$ | reconstructed image |
| $\boldsymbol{y}$ | acquired undersampled data |

Greek Characters

| | |
|---|---|
| $\alpha$ | regularisation parameter |
| $\beta$ | regularisation parameter |
| $\gamma$ | gyromagnetic ratio, rad $s^{-1}$ $T^{-1}$ |
| $\delta$ | gradient pulse length, ms |
| $\Delta$ | observation time, ms |
| $\Delta\omega$ | offset frequency, rad $s^{-1}$ |
| $\tau_c$ | Lagrangian correlation time, s |
| $\phi$ | signal phase, rad |

$\Phi$ bulk signal phase, rad

$\omega$ spin precession frequency, rad $s^{-1}$

Subscripts

*z* axial (*z*) component

**Figure Captions**

**Figure 1:** Schematic of a typical wall-flow filter (not to scale) showing the typical flow features predicted by earlier numerical simulations [8,14,15]. The plugs at the end of the channels extend 0.5 cm into the filter.

**Figure 2:** Schematic diagram showing the DPF sample held inside the PEEK flow cell.

**Figure 3:** Schematic diagram of the recirculating $SF_6$ rig used. (a) compressor, (b) digital pressure gauge, (c) PEEK flow cell contained inside MR spectrometer, (d) mass flow controller. Flow through the rig is counter-clockwise and indicated by the arrows.

**Figure 4:** Schematic of MR pulse sequences used. (a) timing of r.f. pulses and acquisition; (b) slice selection gradients applied along *z*; (c) magnetic field gradients applied along *x*, *y*, and *z*, as required to give spatial resolution along those directions; (d) magnet field gradients applied along *z* for measurement of motion, as used in velocity and turbulent diffusivity measurements.

**Figure 5:** (a) *xz* image of the gas flow velocity along the direction of superficial flow ($v_z$) at the filter entrance for $Re_c = 360$. The image slice thickness is 0.25 cm and the FOV is 1.4 cm (*x*) × 1.7 cm (*z*). Flow profiles along the *x*-axis are shown at *z* = (b) -0.18 cm, (c) +0.02 cm and (d) +0.38 cm relative to the front face of the filter (*z* = 0 cm), with the dashed lines showing $v_z = 0$.

**Figure 6:** *xy* images of $v_z$ at the filter entrance for $Re_c$ = 360. The image slice thickness is 0.25 cm and the FOV is 0.73 cm (*x*) × 0.73 cm (*y*). Images are shown for positions along the length of the filter *z* = (a) -0.38 cm, (b) -0.13 cm, (c) +0.13 cm, (d) +0.38 cm. *z* = 0 defines the entry to the filter.

**Figure 7:** (a) *xz* image of $v_z$ at the filter exit for $Re_c$ = 360. The image slice thickness is 0.25 cm and the FOV is 1.4 cm (*x*) × 1.65 cm (*z*). Flow profiles along the *x*-axis are shown at *z* = (b) -0.02 cm, (c) +0.06 cm and (d) +0.4 cm relative to the rear face of the filter (*z* = 0 cm), with the dashed lines showing $v_z = 0$.

**Figure 8:** *xy* images of $v_z$ showing the expansion of flow and flow heterogeneity at the filter exit for $Re_c$ = 360. The image slice thickness is 0.25 cm and the FOV is 0.9 cm (*x*) × 0.9 cm (*y*). Images are shown for position along the length of the filter *z* = (a) -0.25 cm, (b) +0.25 cm, (c) +0.75 cm, (d) +1.25 cm, (e) + 1.75 cm and (f) +2.25 cm. *z* = 0 defines the filter exit.

**Figure 9:** *xy* images of the turbulent diffusivity at the entrance of the filter for $Re_c$ = 1140 at (a) -0.04, (b) +0.07 and (c) +0.20 cm relative to the front face of the filter (*z* = 0 cm). The voxel slice thickness is 0.13 cm and the FOV is 0.77 cm × 0.77 cm.

**Figure 10:** *xy* images of the turbulent diffusivity at the exit of the filter for $Re_c$ = 1140 at (a) +0.07, (b) +0.2 and (c) +0.33 cm relative to the front face of the filter (*z* = 0 cm). The voxel slice thickness is 0.13 cm and the FOV is 0.77 cm × 0.77 cm.

**Figure 11:** 3D images of $v_z$ and turbulent diffusivity, $D_{turb}$, distributions of gas exiting the filter with $Re_c$ = 1140, coregistered and rendered in Avizo Fire (Fisher Thermo Scientific, USA). The apparently flat profile at the limit of the jets arises from that *z*-position being the limit of the FOV in the imaging experiment.

**Figure 12:** 1D projections of the average turbulent diffusivity at the (a) entrance and (b) exit of the filters onto the *z*-axis for $Re_c$ = 210 (····), 360 (—), 720 (- - -) and 1140 (- . - . -). The vertical dotted lines indicate the limits of the plugged region and $z$ = 0 indicates the respective ends of the filter.

## Table Captions

**Table 1:** Properties of the wall-flow filter.

## References


[1] European Commission, Commission Regulation (EU) No 459/2012 of 29 May 2012 amending Regulation (EC) No 715/2007 of the European Parliament and of the Council and Commission Regulation (EC) No 692/2008 as regards emissions from light passenger and commercial vehicles (Euro 6), 2012.

[2] E.J. Bissett, Mathematical model of the thermal regeneration of a wall-flow monolith diesel particulate filter, Chem. Eng. Sci. 39 (1984) 1233–1244. doi:10.1016/0009-2509(84)85084-8.

[3] G. Koltsakis, O. Haralampous, C. Depcik, J.C. Ragone, Catalyzed diesel particulate filter modeling, Rev. Chem. Eng. 29 (2013) 1–61. doi:10.1515/revce-2012-0008.

[4] F. Sbrizzai, P. Faraldi, A. Soldati, Appraisal of three-dimensional numerical simulation for sub-micron particle deposition in a micro-porous ceramic filter, Chem. Eng. Sci. 60 (2005) 6551–6563. doi:10.1016/j.ces.2005.05.038.

[5] A.J. Torregrosa, J.R. Serrano, F.J. Arnau, P. Piqueras, A fluid dynamic model for unsteady compressible flow in wall-flow diesel particulate filters, Energy. 36 (2011) 671–684. doi:10.1016/j.energy.2010.09.047.

[6] F. Piscaglia, G. Ferrari, A novel 1D approach for the simulation of unsteady reacting flows in diesel exhaust after-treatment systems, Energy. 34 (2009) 2051–2062. doi:10.1016/j.energy.2008.08.022.

[7] M. Schejbal, M. Marek, M. Kubíček, P. Kočí, Modelling of diesel filters for particulates removal, Chem. Eng. J. 154 (2009) 219–230. doi:10.1016/j.cej.2009.04.056.

[8] M. Masoudi, Hydrodynamics of diesel particulate filters, SAE Technical Paper Series (2002) 2002-01-1016. doi:10.4271/2002-01-1016.

[9] T.C. Watling, M.R. Ravenscroft, J.P.E. Cleeton, I.D. Rees, D.A.R. Wilkins, Development of a particulate filter model for the prediction of backpressure: improved momentum balance and entrance and exit effect equations, SAE Int. J. Engines. 10 (2017) 1765-1794. doi:10.4271/2017-01-0974.

[10] R.P. Benedict, J.S. Wyler, J.A. Dudek, A.R. Gleed, Generalized flow across an abrupt enlargement, J. Eng. Power. 98 (1976) 327. doi:10.1115/1.3446171.

[11] F.F. Abdelall, G. Hahn, S.M. Ghiaasiaan, S.I. Abdel-Khalik, S.S. Jeter, M. Yoda, D.L. Sadowski, Pressure drop caused by abrupt flow area changes in small channels, Exp. Therm. Fluid Sci. 29 (2005) 425–434. doi:10.1016/j.expthermflusci.2004.05.001.

[12] P.A. Kolodzie, M. Van Winkle, Discharge coefficients through perforated plates, AIChE J. 3 (1957) 305–312. doi:10.1002/aic.690030304.

[13] P.L. Smith, M. Van Winkle, Discharge coefficients through perforated plates at reynolds numbers of 400 to 3,000, AIChE J. 4 (1958) 266–268. doi:10.1002/aic.690040306.

[14] S. Garimella, W. J. Dowling, M. Van der Veen, and J. D. Killion. The Effect of Simultaneously Developing Flow on Heat Transfer in Rectangular Tubes. Heat Transfer Engineering 22 (2001), 12-25. doi: 10.1080/014576301317048406.

[15] D. West, V. Balakotaiah, Z. Jovanovic. Experimental and theoretical investigation of the mass transfer controlled regime in catalytic monoliths. Catalysis Today 88 (2003),

3-16. doi: 10.1016/j.cattod.2003.08.002.

[16] A.G. Konstandopoulos, E. Skaperdas, M. Masoudi, Inertial contributions to the pressure drop of diesel particulate filters, SAE Technical Paper Series (2001) 2001-01-0909. doi:10.4271/2001-01-0909.

[17] Z.G. Liu, R.K. Miller, Flow distributions and pressure drops of wall-flow diesel particulate filters, SAE Technical Paper Series (2002) 2002-01-1311. doi:10.4271/2002-01-1311.

[18] P.T. Callaghan, Translational Dynamics & Magnetic Resonance: Principles of Pulsed Gradient Spin Echo NMR, 2nd ed., Oxford University Press, 2011.

[19] J.-H. Gao, J.C. Gore, Turbulent flow effects on NMR imaging: Measurement of turbulent intensity, Med. Phys. 18 (1991) 1045–1051. doi:10.1118/1.596645.

[20] J.C. Gatenby, J.C. Gore, Characterization of turbulent flows by NMR measurements with pulsed gradients, J. Magn. Reson. A110 (1994) 26–32. doi:10.1006/jmra.1994.1176.

[21] P.G. de Gennes, Theory of spin echoes in a turbulent fluid, Phys. Lett. 29A (1969) 20–21.

[22] K. Fukuda, A. Hirai, A pulsed NMR study on the flow of fluid, J. Phys. Soc. Japan. 47 (1979) 1999–2006. doi:10.1143/JPSJ.47.1999.

[23] D.O. Kuethe, J.H. Gao, NMR signal loss from turbulence: Models of time dependence compared with data, Phys. Rev. E. 51 (1995) 3252–3262.

doi:10.1103/PhysRevE.51.3252.

[24] E.O. Stejskal, J.E. Tanner, Spin diffusion measurements: Spin echoes in the presence of a time-dependent field gradient, J. Chem. Phys. 42 (1965) 288–292. doi:10.1063/1.1695690.

[25] D.O. Kuethe, Measuring distributions of diffusivity in turbulent fluids with magnetic-resonance imaging, Phys. Rev. A. 40 (1989) 4542–4551. doi:10.1103/PhysRevA.40.4542.

[26] B. Newling, Gas flow measurements by NMR, Prog. Nucl. Magn. Reson. Spectrosc. 52 (2008) 31–48. doi:10.1016/j.pnmrs.2007.08.002.

[27] L.F. Gladden, A.J. Sederman, Recent advances in flow MRI., J. Magn. Reson. 229 (2013) 2–11. doi:10.1016/j.jmr.2012.11.022.

[28] L.F. Gladden, A.J. Sederman, Magnetic resonance imaging and velocity mapping in chemical engineering applications, Annu. Rev. Chem. Biomol. Eng. 8 (2017) 227–247. doi:10.1146/annurev-chembioeng-061114-123222.

[29] M.D. Mantle, A.J. Sederman, L.F. Gladden, S. Raymahasay, J.M. Winterbottom, E.H. Stitt, Dynamic MRI visualization of two-phase flow in a ceramic monolith, AIChE J. 48 (2002) 909–912. doi:10.1002/aic.690480425.

[30] A.J. Sederman, M.D. Mantle, L.F. Gladden, Quantitative “real-time” imaging of multi-phase flow in ceramic monoliths, Magn. Reson. Imaging. 21 (2003) 359–361. doi:10.1016/S0730-725X(03)00138-3.

[31] A.J. Sederman, J.J. Heras, M.D. Mantle, L.F. Gladden, MRI strategies for characterising two-phase flow in parallel channel ceramic monoliths, Catal. Today. 128 (2007) 3–12. doi:10.1016/j.cattod.2007.04.012.

[32] I. Koptyug, S. Altobelli, E. Fukushima, A. Matveev, R. Sagdeev, Thermally polarized $^{1}$H NMR microimaging studies of liquid and gas flow in monolithic catalysts, J. Magn. Reson. 147 (2000) 36–42. doi:10.1006/jmre.2000.2186.

[33] N.P. Ramskill, L.F. Gladden, A.P.E. York, A.J. Sederman, J. Mitchell, K.A. Hardstone, Understanding the operation and preparation of diesel particulate filters using a multi-faceted nuclear magnetic resonance approach, Catal. Today. 216 (2013) 104–110. doi:10.1016/j.cattod.2013.06.023.

[34] N.P. Ramskill, A.P.E. York, A.J. Sederman, L.F. Gladden, Magnetic resonance velocity imaging of gas flow in a diesel particulate filter, Chem. Eng. Sci. 158 (2017) 490–499. doi:10.1016/j.ces.2016.10.017.

[35] A.J. Sederman, M.D. Mantle, C. Buckley, L.F. Gladden, MRI technique for measurement of velocity vectors, acceleration, and autocorrelation functions in turbulent flow, J. Magn. Reson. 166 (2004) 182–189. doi:10.1016/j.jmr.2003.10.016.

[36] A.J. Evans, R.A. Blinder, R.J. Herfkens, C.E. Spritzer, D.O. Kuethe, E.K. Fram, L.W. Hedlund, Effects of turbulence on signal intensity in gradient echo images, Invest. Radiol. 23 (1988) 512–518. doi:10.1097/00004424-198807000-00006.

[37] J.C. Gatenby, J.C. Gore, Mapping of Turbulent Intensity by Magnetic Resonance Imaging, J. Magn. Reson. 104 (1994) 119–126. doi:10.1006/jmrb.1994.1064.

[38] B. Newling, C.C. Poirier, Y. Zhi, J.A. Rioux, A.J. Coristine, D. Roach, B.J. Balcom,

Velocity imaging of highly turbulent gas flow, Phys. Rev. Lett. 93 (2004) 154503. doi:10.1103/PhysRevLett.93.154503.

[39] C.J. Elkins, M.T. Alley, L. Saetran, J.K. Eaton, Three-dimensional magnetic resonance velocimetry measurements of turbulence quantities in complex flow, Exp. Fluids. 46 (2009) 285–296. doi:10.1007/s00348-008-0559-4.

[40] K.R. O'Brien, B.R. Cowan, M. Jain, R.A.H. Stewart, A.J. Kerr, A.A. Young, MRI phase contrast velocity and flow errors in turbulent stenotic jets, J. Magn. Reson. Imaging. 28 (2008) 210–218. doi:10.1002/jmri.21395.

[41] P. Dyverfeldt, R. Gårdhagen, A. Sigfridsson, M. Karlsson, T. Ebbers, On MRI turbulence quantification, Magn. Reson. Imaging. 27 (2009) 913–922. doi:10.1016/j.mri.2009.05.004.

[42] M. Lustig, D. Donoho, J.M. Pauly, Sparse MRI: The application of compressed sensing for rapid MR imaging, Magn. Reson. Med. 58 (2007) 1182–1195. doi:10.1002/mrm.21391.

[43] P. Parasoglou, D. Malioutov, A.J. Sederman, J. Rasburn, H. Powell, L.F. Gladden, A. Blake, M.L. Johns, Quantitative single point imaging with compressed sensing, J. Magn. Reson. 201 (2009) 72–80. doi:10.1016/j.jmr.2009.08.003.

[44] D.J. Holland, D.M. Malioutov, A. Blake, A.J. Sederman, L.F. Gladden, Reducing data acquisition times in phase-encoded velocity imaging using compressed sensing., J. Magn. Reson. 203 (2010) 236–46. doi:10.1016/j.jmr.2010.01.001.

[45] M.H. Sankey, D.J. Holland, A.J. Sederman, L.F. Gladden, Magnetic resonance

velocity imaging of liquid and gas two-phase flow in packed beds., J. Magn. Reson. 196 (2009) 142–8. doi:10.1016/j.jmr.2008.10.021.

[46] D. Xiao, B.J. Balcom, Restricted k-space sampling in pure phase encode MRI of rock core plugs, J. Magn. Reson. 231 (2013) 126–132. doi:10.1016/j.jmr.2013.04.001.

[47] H. Gudbjartsson, S. Patz, The Rician distribution of noisy MRI data, Magn. Reson. Med. 34 (1995) 910–914. doi:10.1002/mrm.1910340618.

[48] D. Strong, T. Chan, Edge-preserving and scale-dependent properties of total variation regularization, Inverse Probl. 19 (2003) S165–S187. doi:10.1088/0266-5611/19/6/059.

[49] M. Benning, L. Gladden, D. Holland, C.B. Schönlieb, T. Valkonen, Phase reconstruction from velocity-encoded MRI measurements - A survey of sparsity-promoting variational approaches, J. Magn. Reson. 238 (2014) 26–43. doi:10.1016/j.jmr.2013.10.003.

[50] M. Mu, X. Li, J. Aslam, Y. Qiu, H. Yang, G. Kou, Y. Wang, A study of shape optimization method on connection cones for diesel particulate filter (DPF), in: Vol. 12 Transp. Syst., ASME, 2016: p. V012T16A001. doi:10.1115/IMECE2016-66080.

[51] L. Ma, M. Paraschivoiu, J. Yao, L. Blackman, Improving flow uniformity in a diesel particulate filter system, SAE Technical Paper Series (2001) 2001-01-1944. doi:10.4271/2001-01-1944.

[52] C. Turner, D. Thornhill, G. McCullough, S. Patel, Comparison of experimental PIV data and CFD simulations for flow in a diesel particulate filter inlet diffuser, SAE Int. J. Engines. 4 (2011) 1556–1570. doi:10.4271/2011-01-1241.

**Tables**

**Table 1:** Properties of the wall-flow filter sample used in the studies.

| **material** | **aluminium titanate** |
|---|---|
| filter channel length / mm | 153 |
| channel width /mm | 1 |
| sample diameter / mm | 15 |
| number of inlet channels | 31 |
| number of outlet channels | 30 |
| wall thickness / mm | 0.33 |
| cell density / cpsi | 300 |
| material porosity / % | 45 |

**Figure 1**

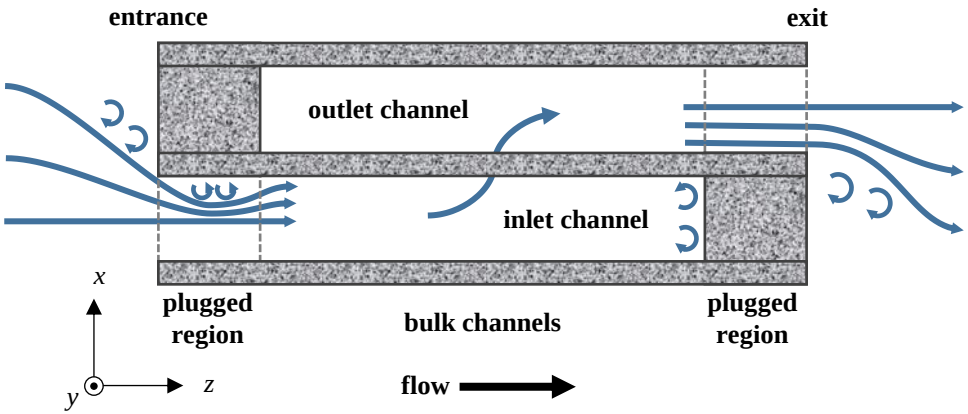
entrance
exit
outlet channel
inlet channel
x
plugged region
bulk channels
plugged region
y
z
flow

**Figure 2**

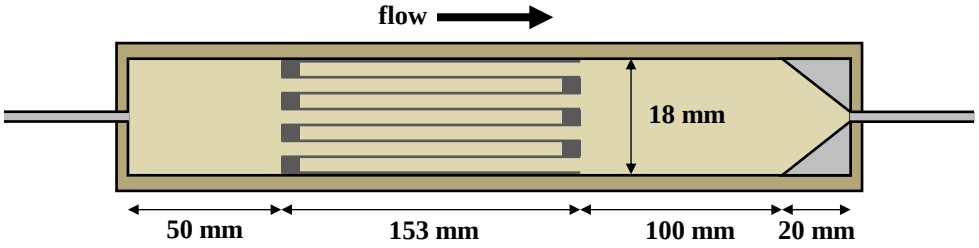

**Figure 3**

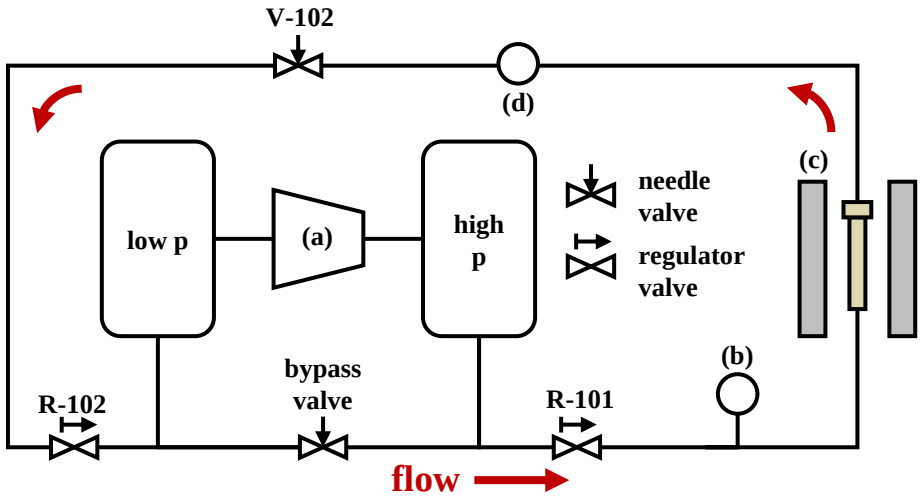
V-102
(d)
low p
(a)
high p
needle valve
regulator valve
(c)
(b)
bypass valve
R-102
R-101
flow

**Figure 4**

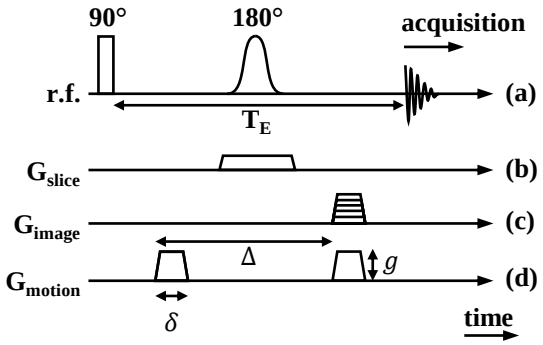
90°
180°
acquisition
r.f.
(a)
$T_E$
$G_{slice}$
(b)
$G_{image}$
(c)
Δ
$g$
$G_{motion}$
(d)
$\delta$
time

**Figure 5**

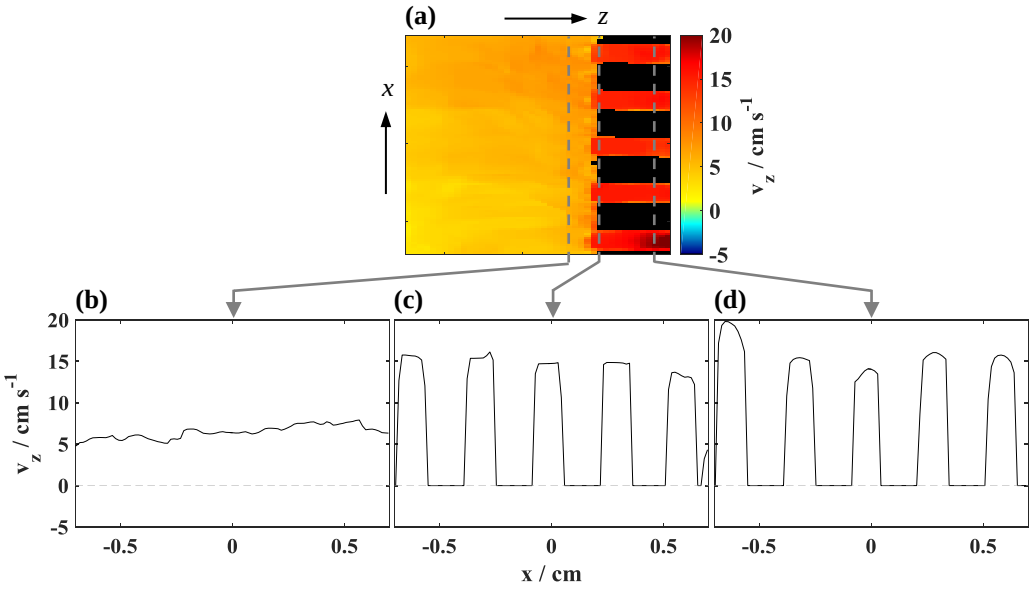

**Figure 6**

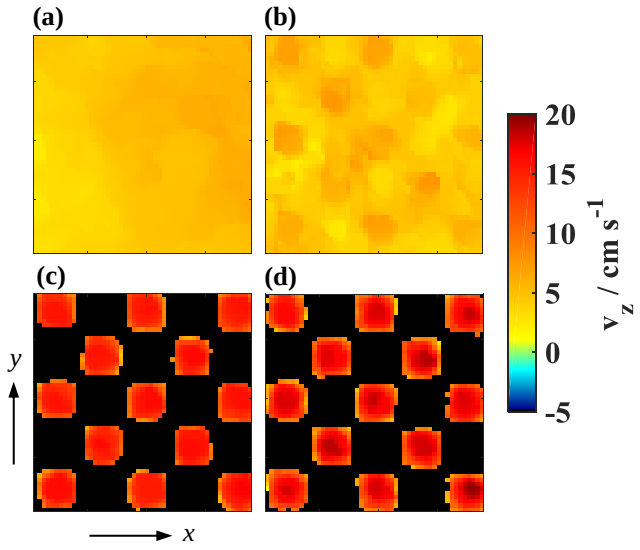

**Figure 7**

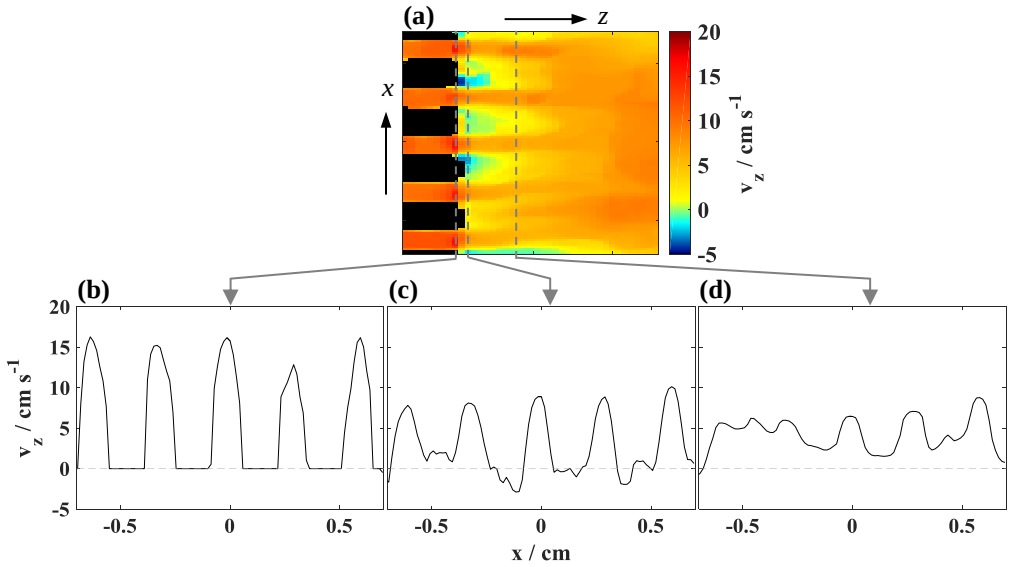

**Figure 8**

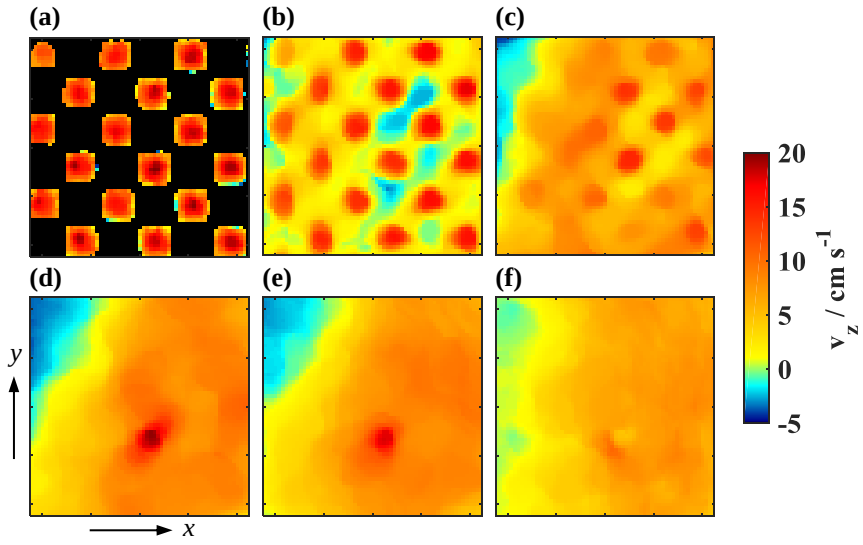

**Figure 9**

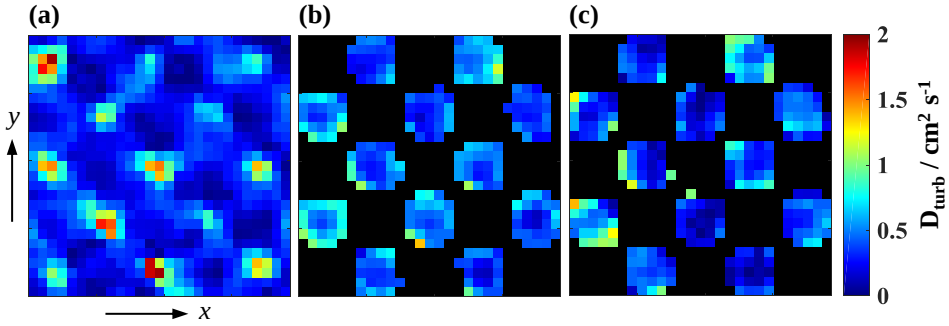

**Figure 10**

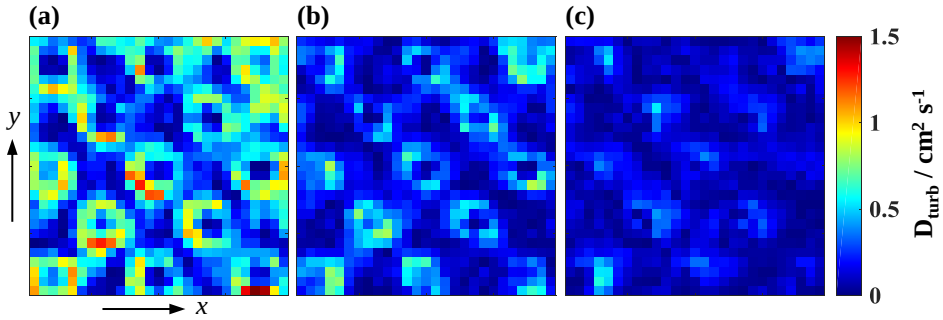

**Figure 11**

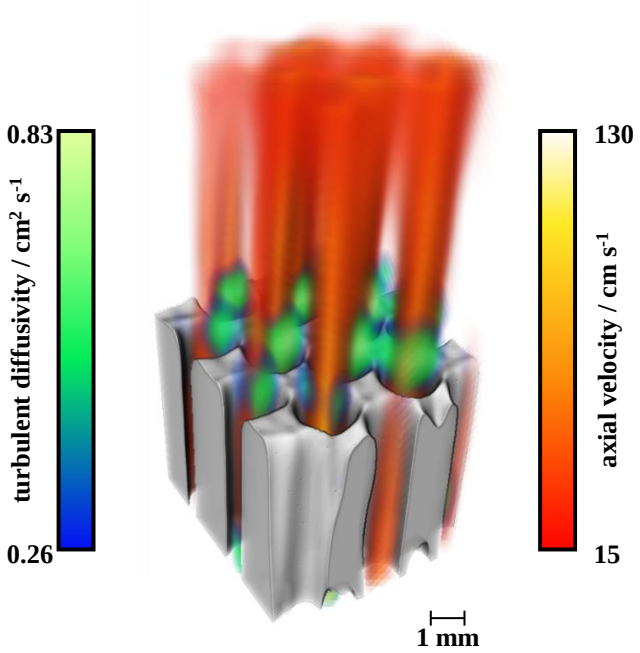
0.83
turbulent diffusivity / cm² s⁻¹
0.26
130
axial velocity / cm s⁻¹
15
1 mm

**Figure 12**

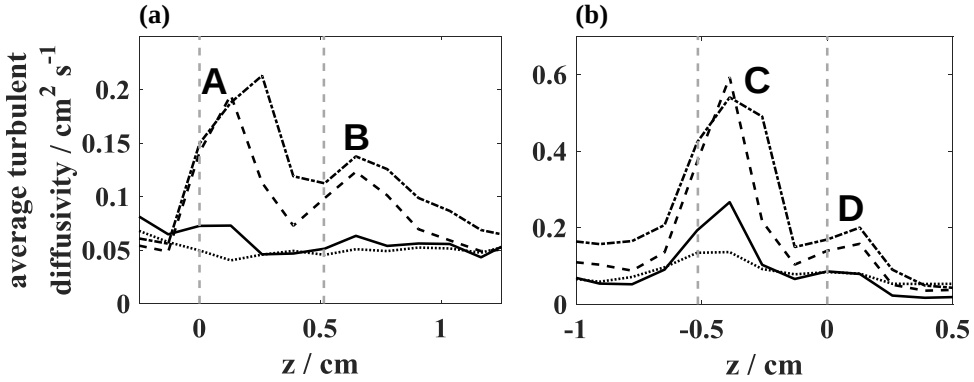
(a)
(b)
A
B
C
D
average turbulent diffusivity / cm$^2$ s$^{-1}$
z / cm
z / cm
0
0.05
0.1
0.15
0.2
0.4
0.6
-1
-0.5
0
0.5
1